ROYAL SOCIETY OF CHEMISTRY

PAPER

Check for updates

Chemical stability of Ca₃Co₄₋ₓO₉₊δ/CaMnO₃₋δ p−n junction for oxide-based thermoelectric generators

Anette Eleonora Gunnæs,[a] Raluca Tofan,[a] Kristian Berland,[a] Sandeep Gorantla,[ab] Thomas Storaas,[a] Temesgen Debelo Desissa, [cd] Matthias Schrade, [ae] Clas Persson,[a] Mari-Ann Einarsrud, [f] Kjell Wiik,[f] Truls Norby[c] and Nikola Kanas [*f]

An all-oxide thermoelectric generator for high-temperature operation depends on a low electrical resistance of the direct p−n junction. $Ca_3Co_{4-x}O_{9+\delta}$ and $CaMnO_{3-\delta}$ exhibit p-type and n-type electronic conductivity, respectively, and the interface between these compounds is the material system investigated here. The effect of heat treatment (at 900 °C for 10 h in air) on the phase and element distribution within this p−n junction was characterized using advanced transmission electron microscopy combined with X-ray diffraction. The heat treatment resulted in counter diffusion of Ca, Mn and Co cations across the junction, and subsequent formation of a $Ca_3Co_{1+y}Mn_{1-y}O_6$ interlayer, in addition to precipitation of Co-oxide, and accompanying diffusion and redistribution of Ca across the junction. The Co/Mn ratio in $Ca_3Co_{1+y}Mn_{1-y}O_6$ varies and is close to 1 ($y = 0$) at the $Ca_3Co_{1+y}Mn_{1-y}O_6–CaMnO_{3-\delta}$ boundary. The existence of a wide homogeneity range of $0 \leq y \leq 1$ for $Ca_3Co_{1+y}Mn_{1-y}O_6$ is corroborated with density functional theory (DFT) calculations showing a small negative mixing energy in the whole range.

Introduction

For waste heat harvesting at high temperatures and oxidizing conditions, thermoelectric generators (TEGs) based on oxides represent an interesting technology, enabling increased energy efficiency of any high-temperature process where heat harvesting is viable.[1] Oxide-based thermoelectrics exhibit modest efficiencies compared with state-of-the-art non-oxides, but offer in principle superior stability at high temperatures in air (oxidizing conditions). The stability is however jeopardized by the need for metallic interconnects to form well-conducting contacts between the oxide p- and n-type legs, since the metals are noble (rare and expensive) or they will oxidize over time. Cracking or exfoliation due to differences in coefficients of thermal expansion (CTEs) between ceramic conductors and metal interconnects represent additional challenges.[2] TEGs with direct contact between the p- and n-type legs without metallic interconnects in between have however been proposed.[3–5] By avoiding the metallic interconnects,

manufacturing becomes both simpler and less expensive. Such a direct oxide p−n junction faces however not only challenges in terms of high contact resistances from charge carrier depletion, but also stability issues related to interdiffusion and formation of new phases at the interface region. These stability issues are addressed in the present investigation for the specific case of $Ca_3Co_{4-x}O_{9+\delta}–CaMnO_{3-\delta}$.

The recently reported all-oxide TEG made of p-type $Ca_3Co_{4-x}O_{9+\delta}$ and n-type $CaMnO_{3-\delta}$ introduced a new concept where a new phase with favorable thermoelectric properties is formed *in situ* at the interface between the p- and n-type conductors.[6] Herein, we further study the materials and present a detailed analysis of the interdiffusion and formation of the secondary phases at the p−n interface in air and typical operating temperature of 900 °C.

According to Woermann *et al.*, $Ca_3Co_{4-x}O_{9+\delta}$ is stable up to 926 °C in air, at which it decomposes to $Ca_3Co_2O_6$ and a $Co_{1-z}Ca_zO$ (ss).[7] $Ca_3Co_{4-x}O_{9+\delta}$ is described with a homogeneity range ($Ca_3Co_{3.9+x}O_{9+\delta}$) with x between −0.03 and +0.17 at 900 °C.[8] The homogeneity range increases towards Co-rich compositions with increasing temperatures and becomes narrowly sharp, where it ends at a single point.[8] The stoichiometry of $Ca_3Co_{4-x}O_{9+\delta}$ in our investigation corresponds to x within the homogeneity range as mentioned above, giving a maximum operating temperature of 900 °C.[6,8,9]

$Ca_3Co_{4-x}O_{9+\delta}$ has a superlattice-misfit structure consisting of two monoclinic subsystems: a triple rock salt (RS)-type slab of Ca_2CoO_3 and a single CdI_2-type CoO_2 slab. The subsystems have

ᵃDepartment of Physics, University of Oslo, SMN, FERMiO, NO-0349 Oslo, Norway

ᵇŁUKASIEWICZ Research Network – PORT Polish Center for Technology Development, 54-066 Wrocław, Poland

ᶜDepartment of Chemistry, University of Oslo, SMN, FERMiO, NO-0349 Oslo, Norway

ᵈDepartment of Materials Science and Engineering, Adama Science and Technology University, 1888 Adama, Ethiopia

ᵉDepartment of Sustainable Energy Technology, SINTEF, 0314 Oslo, Norway

ᶠDepartment of Material Science and Engineering, NTNU Norwegian University of Science and Technology, 7491 Trondheim, Norway. E-mail: nikola.kanas@ntnu.no

identical a, c, and β parameters, but different b parameters: $a = 4.8376$ Å, $c = 10.833$ Å, $\beta = 98.06$, $b_1 = 4.5565$ Å, and $b_2 = 2.8189$ Å.[10–13]

CaMnO$_{3-\delta}$ has an orthorhombic perovskite type structure, with lattice constants $a = 5.279$ Å, $b = 7.448$ Å and $c = 5.264$ Å at room temperature.[14] Upon heating in air, the oxygen content is reduced and structural phase transitions occur at 893 and 913 °C with resulting tetragonal and cubic structural modifications, respectively.[15] However, the phase transition temperatures are strongly dependent on the oxygen stoichiometry.[16] According to the CaMnO$_{3-\delta}$ phase diagram the cubic-to-tetragonal and tetragonal-to-orthorhombic transformations occur when $3 - \delta \approx 2.965$ and 2.98, respectively, at 900 °C.[17] Oxygen stoichiometry in air is reported to be 2.94 at 900 °C,[17] and hence CaMnO$_{3-\delta}$ should be in the cubic phase domain considering the heat treatment used in this work.

Golovkin *et al.* have reported phase diagrams of the system Ca–Mn–Co–O.[18] Ca$_3$Co$_{4-x}$O$_{9+\delta}$ exhibits a certain solid solubility of Mn,[19,20] and the formation of a quaternary phase Ca$_3$Co$_{1+y}$Mn$_{1-y}$O$_6$ is described by several authors.[21–23] This phase has been reported to have a K$_4$CdCl$_6$ type of structure, the same as the pristine Ca$_3$Co$_2$O$_6$ phase, with space group $R\bar{3}c$. Both Hervoches *et al.*[22] and Kanas *et al.*[24] have confirmed a wide homogeneity range for Ca$_3$-Co$_{1+y}$Mn$_{1-y}$O$_6$, extending from $y = 0$ to 1.

To establish all-oxide thermoelectric generators for operation in air at high temperatures, a detailed understanding of the processes taking place at the p–n junction at typical operating temperatures is decisive. In this investigation, we present a comprehensive study of the interdiffusion and formation of secondary phases at the Ca$_3$Co$_{4-x}$O$_{9+\delta}$/CaMnO$_{3-\delta}$ interface in air at 900 °C.

Results and discussion

The SEM cross section view of the specimen in Fig. 1 shows the interface between the relatively dense CaMnO$_{3-\delta}$ and the porous Ca$_3$Co$_{4-x}$O$_{9+\delta}$ layer after heat treatment at 900 °C for 10 h. The distribution of Co (pink), Mn (blue) and Ca (green) at and in the vicinity of the interface between Ca$_3$Co$_{4-x}$O$_{9+\delta}$ and CaMnO$_{3-\delta}$ is visualized in the bottom left inset in Fig. 1.

Two distinctly different regions are identified at the junction: "Region (a)" which is a ∼10 μm thick porous region at the porous Ca$_3$Co$_{4-x}$O$_{9+\delta}$ side with a high density of Co-rich grains (pink in Fig. 1, bottom right inset).

"Region (b)" is a ∼2 μm thick dense interphase region with a significantly higher Ca/Mn ratio compared to the bulk CaMnO$_{3-\delta}$ (green layer in Fig. 1, bottom right inset). Chemical analysis, topographically performed across the junction (Fig. 2), is in agreement with the observations from Fig. 1. The variations in the concentration of Ca, Mn and Co across the interface are given in Fig. 2b. Mn is seen to diffuse far into the porous Ca$_3$Co$_{4-x}$O$_{9+\delta}$, while the Mn concentration in Region (b) is lower than in the main bulk phase of CaMnO$_{3-\delta}$. Enhanced level of Ca is observed in Region (b) (interphase region) while a depletion in Ca is obvious in Region (a) (porous region). There is a moderate gradient in the Co concentration all through the Ca$_3$Co$_{4-x}$O$_{9+\delta}$ layer until we reach the boundary between Region (a) and (b), followed by a steep decrease across Region (b).

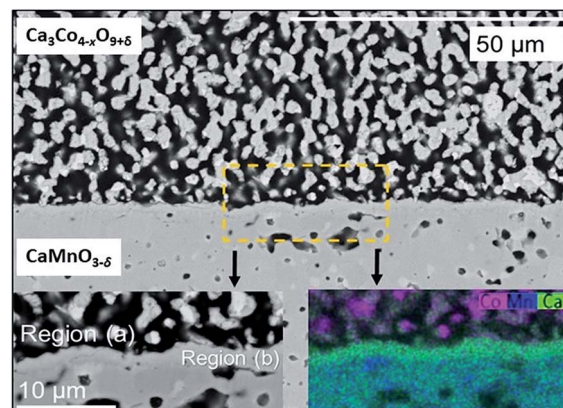**Fig. 1** SEM micrograph of a cross section of the Ca$_3$Co$_{4-x}$O$_{9+\delta}$/CaMnO$_{3-\delta}$ interface after heat treatment at 900 °C for 10 h. The bottom insets correspond to a magnification of the rectangular stippled area, where bottom left is the SEM-image and bottom right corresponds to an EDS map of Ca (green), Mn (blue) and Co (pink). Region (a) corresponds to the porous region in the vicinity of the interface, while Region (b) corresponds to the interphase region, in-between the initial phases Ca$_3$Co$_{4-x}$O$_{9+\delta}$ and CaMnO$_{3-\delta}$.

Co is also seen to diffuse rather far into the CaMnO$_{3-\delta}$ phase. This is in agreement with our recent data on bulk and enhanced grain boundary diffusivity of Co into CaMnO$_{3-\delta}$,[25] where the bulk diffusivity at 900 °C would predict a diffusion length of 0.1 μm, while the enhanced grain boundary diffusion can explain the length closer to 10 μm in Fig. 2b. The faster diffusion of Mn into Ca$_3$Co$_{4-x}$O$_{9+\delta}$ is most probably related to the porosity promoting enhanced surface diffusion. After careful surface polishing from the Ca$_3$Co$_{4-x}$O$_{9+\delta}$ side (Fig. 3a), the polished surface was subjected to SEM/EDS analysis.

EDS elemental maps were taken along the surface (4 lowermost sections in Fig. 3b) and quantitative EDS analyses were made at 6 positions ("spots") according to the numbering given in Fig. 3b (uppermost section). The results of the quantitative
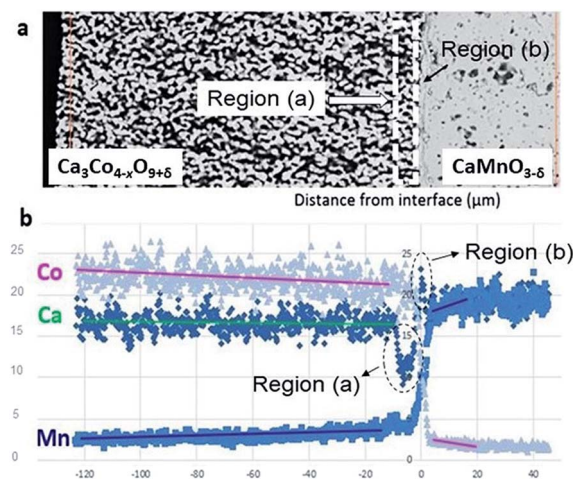

Fig. 2 (a) SEM micrograph of the area analyzed by EDS. (b) Corresponding EDS diffusion profiles of Co, Mn and Ca. Unit of abscissa in μm and unit of ordinate in at%.
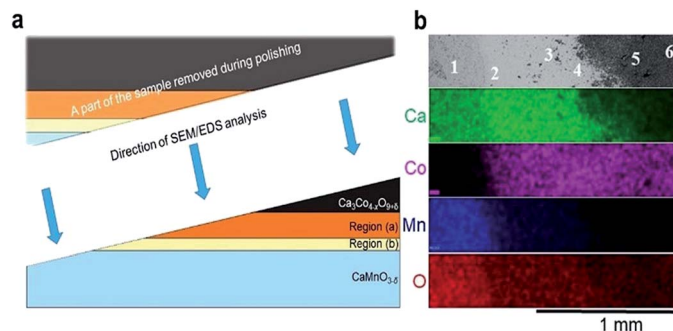
Fig. 3 (a) A schematic illustration of the polished sample prior to SEM/EDS analysis. The figure is not drawn to scale, and Regions (a) and (b) are extended for the sake of clarity. (b) Plane view of back scattered electron image (uppermost section) followed by corresponding EDS maps of Ca (green), Co (pink), Mn (blue) and O (red). The assessment of the chemical composition was supplemented by spot EDS analysis according to the positions numbered from 1 to 6 in the uppermost section, and the results are given in Table 1.

EDS analysis are given in Table 1. The compositions in positions 1 and 5 correspond to $CaMnO_{3-\delta}$ and $Ca_3Co_{4-x}O_{9+\delta}$, respectively, while position 6 most probably correspond to mixture of $Ca_3Co_{4-x}O_{9+\delta}$ and Co_3O_4. Position 3 (Region (b)) correspond to the quaternary phase, $Ca_3Co_{1+y}Mn_{1-y}O_6$,[22–24] where the ratio between Ca and the sum of Mn and Co is 1.53 which is close to 1.5 as expected in $Ca_3Co_{1+y}Mn_{1-y}O_6$. We suggest that position 4 is representative for the porous region (Region (a)) due to the ratio Ca/(Mn + Co) is 1.33, which is between $Ca_3Co_{4-x}O_{9+\delta}$ (≈ 0.75) and $Ca_3Co_{1+y}Mn_{1-y}O_6$ (1.53), hence a mixture of $Ca_3Co_{1+y}Mn_{1-y}O_6$ and $Ca_3Co_{4-x}O_{9+\delta}$. Position 2 shows a cation ratio between $CaMnO_{3-\delta}$ and $Ca_3Co_{1+y}Mn_{1-y}O_6$ and may be a mix of these two phases. It should be emphasized that there are uncertainties related to these calculations, both in the accuracy of the measurement as well as the fact that spot analysis also may include elements from phases below the point of analysis. Besides Ca redistribution, a thin densified reaction layer of $Ca_3Co_{1+y}Mn_{1-y}O_6$ is formed as a result of Co entering into $CaMnO_{3-\delta}$. Variations in the Co/Mn ratio across the $Ca_3Co_{1+y}Mn_{1-y}O_6$ reaction layer is expected as this forms a diffusion barrier for both cations and allows a wide range of mixing ratios, as seen from the steepness of both the Mn- and Co-profiles in Region (b) (Fig. 2).

Besides, a thermopower across the $Ca_3Co_{1+y}Mn_{1-y}O_6$ reaction layer in TEG is directly affected by the Co/Mn ratio in $Ca_3Co_{1+y}Mn_{1-y}O_6$, where the thermopower increases as Co/Mn ratio decreases.[24]

The polished plane view surface was further analyzed by XRD for phase clarification, where the main reflections corresponded to $CaMnO_{3-\delta}$ and $Ca_3Co_{4-x}O_{9+\delta}$ (Fig. 4).

With respect to the annealing temperature (900 °C), which is close to the Co_3O_4/CoO phase transition in air,[26] Co will definitely be oxidized during cooling and at room temperature to exist as Co_3O_4. The broad and unsymmetrical set of reflections marked with "*" fits well to the trigonal structure of $Ca_3Co_{1+y}Mn_{1-y}O_6$ with space group $R\bar{3}c$.[22] These results are in good agreement with our EDS compositional analysis (Fig. 3 and Table 1).

A detailed TEM/EDS analysis of the interface between $CaMnO_{3-\delta}$ and Region (b) is presented in Fig. 5, where (a) to (d) are STEM-image and EDS analysis, while (e) and (f) are TEM-image and SAD zone axis patterns, respectively. The most striking feature is the sharp boundary between $CaMnO_{3-\delta}$ and Region (b) shown by the yellow line in Fig. 5(e). Above the yellow line the $Ca_3Co_{1+y}Mn_{1-y}O_6$ phase is confirmed by the SAD [12−1] zone axis patterns shown in (f), and further supported by the EDS analysis in (b)–(d) showing the presence of Ca, Co and Mn. The absence of Co and presence of Ca and Mn below the yellow line ((b)–(d)) confirm the presence of only $CaMnO_{3-\delta}$ in this region. Although we expect some diffusion of Co into the

Table 1 at% of cations at the spots given in Fig. 3. The uncertainties in Ca, Co and Mn are ± 1 at%, while for O it is ± 5 at% and is due to the inherent accuracy of the EDS method. The phases dominating at the various spots are suggested based on the ratio between the cations. Also included is the expected ratio between the cations (Ca/(Mn + Co)) in stoichiometric $CaMnO_{3-\delta}$, $Ca_3Co_{1+y}Mn_{1-y}O_6$ and $Ca_3Co_{4-x}O_{9+\delta}$, respectively

Spot	Ca	Co	Mn	O	Co + Mn	Ca/(Co + Mn)	Phase	Region
1	20	0–1	20	60	20	1.00	$CaMnO_{3-\delta}$	—
2	28	6	14	53	20		$CaMnO_{3-\delta}$/$Ca_3Co_{1+y}Mn_{1-y}O_6$	—
3	29	11	8	53	19		$Ca_3Co_{1+y}Mn_{1-y}O_6$	(b)
4	28	13	8	52	21		$Ca_3Co_{1+y}Mn_{1-y}O_6$/$Ca_3Co_{4-x}O_{9+\delta}$	(a)
5	20	22	3	57	25		$Ca_3Co_{4-x}O_{9+\delta}$	—
6	16	23	2	60	25		$Ca_3Co_{4-x}O_{9+\delta}$	—
$CaMnO_{3-\delta}$						1		—
$Ca_3Co_{1+y}Mn_{1-y}O_6$						1.5		—
$Ca_3Co_{4-x}O_{9+\delta}$						0.75		—

Paper

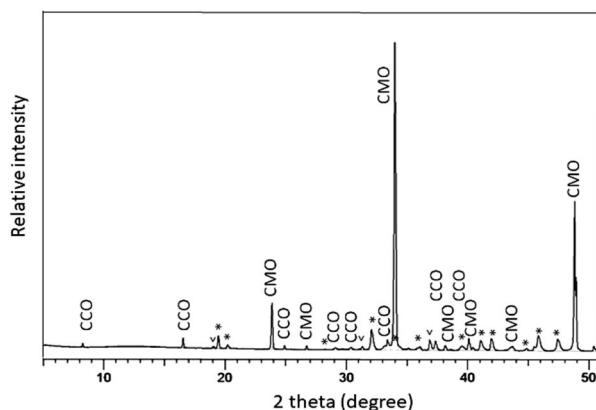**Fig. 4** XRD diffractogram of the polished top view surface at the interface between $CaMnO_{3-\delta}$ and $Ca_3Co_{4-x}O_{9+\delta}$. The reflections marked with "*" and "v" are due to the presence of $Ca_3Co_{1+y}Mn_{1-y}O_6$ and Co_3O_4, respectively. $CaMnO_{3-\delta}$ is identified as the low temperature (LT) orthorhombic phase while $Ca_3Co_{1+y}Mn_{1-y}O_6$ fits well with a trigonal structure with space group $R3c$. $CaMnO_{3-\delta}$ and $Ca_3Co_{4-x}O_{9+\delta}$ are marked as (CMO) (CCO), respectively.

$CaMnO_{3-\delta}$ phase (Fig. 2), the concentration is below the detection limit in (d).

The $CaMnO_{3-\delta}$ grains are identified as the low temperature (LT) orthorhombic $CaMnO_{3-\delta}$ phase (Fig. 4) and the appearance of the $CaMnO_{3-\delta}$ grains in Fig. 5(e) indicate high defect concentration appearing as a line pattern.

The high defect concentration is probably due to tensile stresses in $CaMnO_{3-\delta}$ originating from the phase transition between the high temperature cubic phase (HT) to the LT phase, which is followed by a significant volume contraction.

A detailed TEM/EDS analysis of Region (a) is given in Fig. 6. The EDS analysis in Fig. 6(c) confirms the formation of a Co-oxide rich phase, however connected to a phase containing Ca, Co and Mn. SAD [12−1] zone axis patterns identified this phase to be $Ca_3Co_{1+y}Mn_{1-y}O_6$ (Fig. 6(d)) showing that $Ca_3Co_{1+y}Mn_{1-y}O_6$ also may be formed quite far from the initial interface between $Ca_3Co_{4-x}O_{9+\delta}$ and $CaMnO_{3-\delta}$. The reason for the formation of $Ca_3Co_{1+y}Mn_{1-y}O_6$ far into Region (a) is a combination of Co depletion of the $Ca_3Co_{4-x}O_{9+\delta}$ phase, due to diffusion of Co towards $CaMnO_{3-\delta}$, and counter diffusion of Mn into the $Ca_3Co_{4-x}O_{9+\delta}$ phase (some solid solubility[19,20]). At some critical composition, $Ca_3Co_{4-x}O_{9+\delta}$ will decompose and form $Ca_3Co_{1+y}Mn_{1-y}O_6$ and a Co-oxide rich phase. The depletion of Ca in Region (a) (Fig. 2b) suggests that Ca diffuses towards Region (b), which is intuitively surprising since diffusion seemingly takes place against its concentration gradient.

However, assuming that the thermodynamic activity (chemical potential) of calcium in the $Ca_3Co_{4-x}O_{9+\delta}$-phase is much higher than in the $Ca_3Co_{1+y}Mn_{1-y}O_6$-phase there will be a thermodynamic driving force for Ca-diffusion from Region (a) to Region (b). This explains the enhanced Ca concentration in Region (b) and Ca depletion in Region (a) (Fig. 2b). However, the formation of $Ca_3Co_{1+y}Mn_{1-y}O_6$ depends on diffusion of Mn through the increasing layer of dense $Ca_3Co_{1+y}Mn_{1-y}O_6$, which is expected to follow the parabolic law. Hence, the formation of $Ca_3Co_{1+y}Mn_{1-y}O_6$ will

virtually stop with time, corresponding to a fixed thickness of the $Ca_3Co_{1+y}Mn_{1-y}O_6$ layer. The effect of counter diffusion and the formation of $Ca_3Co_{1+y}Mn_{1-y}O_6$ on TEG performance is thoroughly elaborated in a previous paper by Kanas et al.[6] $Ca_3Co_{1+y}Mn_{1-y}O_6$ forms together with $Ca_3Co_{4-x}O_{9+\delta}$ and $CaMnO_{3-\delta}$ a p–p–n junction which exhibits ohmic behavior and a transverse thermoelectric effect, boosting the open-circuit voltage of the module. Furthermore, the electron energy levels of $Ca_3Co_{1+y}Mn_{1-y}O_6$ are located intermediate of those of $Ca_3Co_{4-x}O_{9+\delta}$ and $CaMnO_{3-\delta}$, which reduces the depletion of charge carriers at the $Ca_3Co_{4-x}O_{9+\delta}$–$Ca_3Co_{1+y}Mn_{1-y}O_6$ and $Ca_3Co_{1+y}Mn_{1-y}O_6$–$CaMnO_{3-\delta}$ interfaces, as compared to initial $Ca_3Co_{4-x}O_{9+\delta}$–$CaMnO_{3-\delta}$ p–n interface.[6]

DFT results for the mixing energy of $Ca_3Co_{1+y}Mn_{1-y}O_6$ depicted in Fig. 7 show small negative values for the entire composition range, with a shallow minimum at $y = 0.25$, corresponding to a mixing energy of -5 meV per formula unit. According to the DFT calculations the most stable $Ca_3Co_{1+y}Mn_{1-y}O_6$ composition should be in the vicinity of $y \sim 0.25$, corresponding to a [Co]/[Mn] ratio of ~ 1.67.

Nevertheless, the negative mixing energy obtained in the entire range from $y = 0.1$ to 0.9 supports the existence of solid solubility in the whole range from $y = 0$ to 1, as confirmed by Hervoches et al.[22] and Kanas et al.[24] A small mixing energy is reasonable given that Co and Mn have similar atom sizes, and the DFT result serves to confirm that the nature of chemical bonding is not greatly affected by the substitution. At finite temperature the free energy would clearly show a broad minimum dominated by the entropy term which was not considered in these 0 K calculations.

All in all, the comprehensive structural analysis of the $Ca_3Co_{4-x}O_{9+\delta}$/$CaMnO_{3-\delta}$ p–n junction gives an important overview of the complexity, described by counter diffusion and formation of several reaction products at the interface. In high-
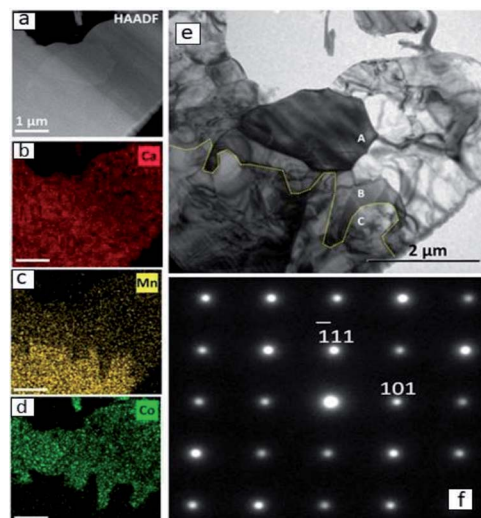

Fig. 5 (a) STEM and (e) TEM images of Region (b) connected to $CaMnO_{3-\delta}$ with the corresponding EDS maps of (b) Ca, (c) Mn and (d) Co. The yellow line in (e) marks the interface between $CaMnO_{3-\delta}$ (lower part) and $Ca_3Co_{1+y}Mn_{1-y}O_6$ (upper part). SAD [12−1] zone axis patterns of regions above the yellow line (grain A and B) confirm the presence of $Ca_3Co_{1+y}Mn_{1-y}O_6$ and an example is shown in (f).

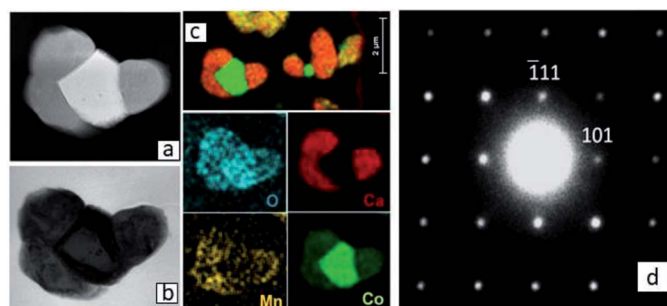**Fig. 6** (a) HAADF STEM and (b) TEM images of connected $Ca_3Co_{1+y}Mn_{1-y}O_6$ and CoO core/Co_3O_4 shell grains in Region (a) quite far from the original $Ca_3Co_{4-x}O_{9+\delta}$–$CaMnO_{3-\delta}$ interface, with (c) corresponding EDS maps. (d) SAD [12−1] zone axis patterns of $Ca_3Co_{1+y}Mn_{1-y}O_6$ from Region (a).
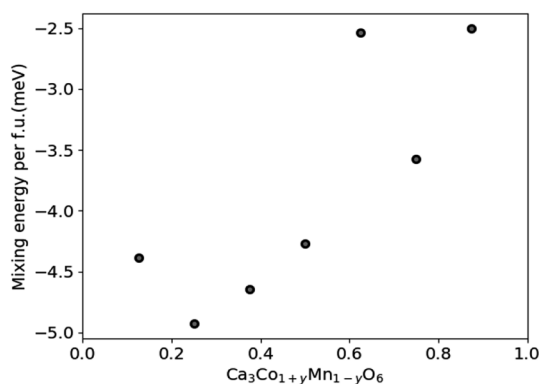

Fig. 7 Calculated mixing energies of $Ca_3Co_{1+y}Mn_{1-y}O_6$ as a function of y in $Ca_3Co_{1+y}Mn_{1-y}O_6$. The scatter may reflect the limited size and number of atoms of the computational cell.

temperature applications the hot side of this TEG boosts the overall performance through a high open circuit voltage which occurs due to counter diffusion of cations resulting in formation of $Ca_3Co_{1+y}Mn_{1-y}O_6$ with a high thermopower.[6,24]

Conclusions

The $Ca_3Co_{4-x}O_{9+\delta}$/$CaMnO_{3-\delta}$ p–n junction is not stable at 900 °C as a new $Ca_3Co_{1+y}Mn_{1-y}O_6$ intermediate phase forms through counter diffusion of Ca, Co and Mn. On the $CaMnO_{3-\delta}$ side, a thin dense layer of $Ca_3Co_{1+y}Mn_{1-y}O_6$ with variable composition forms, in which further in-diffusion of Co is slow. On the $Ca_3Co_{4-x}O_{9+\delta}$ side, Mn diffusion into $Ca_3Co_{4-x}O_{9+\delta}$ together with Co deficiency gives decomposition into $Ca_3Co_{1+y}Mn_{1-y}O_6$ and Co-oxide. The diffusion profiles are in qualitative agreement with our recently published data on Co diffusion in $CaMnO_{3-\delta}$. DFT calculations and experimental evidence support the wider homogeneity range ($0 \leq y \leq 1$) of $Ca_3Co_{1+y}Mn_{1-y}O_6$.

Experimental

Phase-pure $CaMnO_{3-\delta}$ powder was synthesized by solid-state reaction using a stoichiometric ratio of $CaCO_3$ (Inframat Advanced Materials, >99% purity) and MnO_2 (Sigma Aldrich, >99% purity) precursors, mixed and heated twice at 1200 °C for 14 h in air with grinding in between. A dense $CaMnO_{3-\delta}$ pellet (diameter 12 mm, thickness 4 mm) was formed by cold isostatic pressing (CIP) at 200 MPa followed by sintering at 1300 °C for 14 h in air using a heating rate of 200 K h^{-1} and cooling rate of 100 K h^{-1}. The dense $CaMnO_{3-\delta}$ pellet was ground and polished with SiC papers and diamond paste to 1 μm. $Ca_3Co_{4-x}O_{9+\delta}$ powder, with the nominal stoichiometry $Ca_3Co_4O_{9+\delta}$, was prepared by spray pyrolysis (CerPoTech AS, Norway), and a $Ca_3Co_{4-x}O_{9+\delta}$ layer was produced by tape casting according to ref. 6. The tape was cast, laminated, and attached onto the polished $CaMnO_{3-\delta}$ surface by pressing at 10 MPa and 80 °C for 3 min. The sample was then calcined at 450 °C for 1 h in air to remove organics and further heated at 900 °C for 10 h. Firm adhesion between $Ca_3Co_{4-x}O_{9+\delta}$ and $CaMnO_{3-\delta}$ was obtained after the heat treatment.

The sample was subsequently embedded in epoxy and divided in pieces for both cross section and plane view examinations. The specimens were ground with SiC paper, and final polishing was done with colloidal Al_2O_3 (0.05 μm). For the plane view examination, the specimen was polished down stepwise from the $Ca_3Co_{4-x}O_{9+\delta}$ side. The exposed area was analyzed by scanning electron microscopy (SEM) with energy dispersive X-ray energy dispersive spectroscopy (EDS) and X-ray diffraction (XRD) in between each polishing step. Cross section specimens were examined by a combination of SEM and transmission electron microscopy (TEM) enabling structural studies at both micro- and nanoscale. The TEM specimen, covering a ~15 μm long region across the $CaMnO_{3-\delta}$/$Ca_3Co_{4-x}O_{9+\delta}$ interface, was cut out by use of a focused ion beam (FIB) and thinned down to about 100 nm. EDS was conducted to map and quantify the elemental composition globally and locally by SEM and TEM, respectively. To improve statistics, line scan data sets were added after aligning the onset of the dense interface region.

A Rigaku MiniFlex600 system using Cu Kα radiation and florescence correction was used for the XRD investigation, while a Hitachi TM3000 SEM, a JEOL2010F TEM operated at 200 kV and a Cs probe corrected FEI Titan G2 60-300 TEM operated at 300 kV were used for the SEM and TEM studies.

The mixing energy of $Ca_3Co_{1+y}Mn_{1-y}O_6$ was calculated within the spin-polarized density functional theory (DFT) utilizing the projector-augmented-plane wave method as implemented in VASP,[27,28] and choosing the generalized-gradient approximation functional PBE.[29] A supercell consisting of $2 \times 2 \times 2$ primitive unit cells was used to emulate the solid solution, which was set up by randomly replacing 2, 4, 6, 8, 10, 12, and 14 of the 16 Mn atoms with Co atoms in the $Ca_3Co_{1+y}Mn_{1-y}O_6$ supercell. To obtain an estimate of the mixing energy, we rely on a ferromagnetic ordering with spin aligned in intra-chain (111) direction. The plane-wave energy cutoff was set to 520 eV with a $2 \times 2 \times 2$ Monkhorst–Pack k-point sampling of the Brillouin zone. Atomic coordinates and unit cell were relaxed until the total energy varied by less than 0.03 meV per formula unit.

Conflicts of interest

There are no conflicts to declare.

Acknowledgements

References

1 S. Twaha, J. Zhu, Y. Yan and B. Li, *Renewable Sustainable Energy Rev.*, 2016, **65**, 698–726.

2 W. Liu, Q. Jie, S. E. Kim and Z. Ren, *Acta Mater.*, 2015, **87**, 357–376.

3 A. Becker, R. Chavez, N. Petermann, G. Schierning and R. Schmechel, *J. Electron. Mater.*, 2013, **42**, 2297–2300.

4 R. Chavez, S. Angst, J. Hall, F. Maculewicz, J. Stoetzel, H. Wiggers, L. T. Hung, N. Van Nong, N. Pryds, G. Span, D. E. Wolf, R. Schmechel and G. Schierning, *J. Phys. D Appl. Phys.*, 2018, **51**, 014005.

5 G. Span, M. Wagner, S. Holzer and T. Grasser, *25th International Conference on Thermoelectrics*, ICT, Vienna, 6–10 August, 2006.

6 N. Kanas, M. Bittner, S. P. Singh, T. D. Desissa, T. Norby, A. Feldhoff, T. Grande, K. Wiik and M.-A. Einarsrud, *ACS Omega*, 2018, **3**, 9899–9906.

7 E. Woermann and A. Muan, *J. Inorg. Nucl. Chem.*, 1970, **32**, 1455–1459.

8 D. Sedmidubsky, V. Jakes, O. Jankovsky, J. Leitner, Z. Sofer and J. Hejtmanek, *J. Solid State Chem.*, 2012, **194**, 199–205.

9 N. Kanas, S. P. Singh, M. Rotan, M. Saleemi, M. Bittner, A. Feldhoff, T. Norby, K. Wiik, T. Grande and M.-A. Einarsrud, *J. Eur. Ceram. Soc.*, 2018, **38**, 1592–1599.

10 Y. Miyazaki, *Solid State Ionics*, 2004, **172**, 463–467.

11 Y. Miyazaki, M. Onoda, T. Oku, M. Kikichi, Y. Ishii, Y. Ono, Y. Morii and T. Kajitani, *J. Phys. Soc. Jpn.*, 2002, **71**, 491–497.

12 A. C. Masset, C. Michel, A. Maignan, M. Hervieu, O. Toulemonde, F. Studer and B. Raveau, *Phys. Rev. B: Condens. Matter Mater. Phys.*, 2000, **62**, 166–175.

13 M. Schrade, H. Fjeld, T. G. Finstad and T. Norby, *J. Phys. Chem. C*, 2014, **118**, 2908–2918.

14 K. R. Poeppelmeier, M. E. Leonowicz, J. C. Scanlon, J. M. Longo and W. B. Yelon, *J. Solid State Chem.*, 1982, **45**, 71–79.

15 H. Taguchi, M. Nagao, T. Sato and M. Shimada, *J. Solid State Chem.*, 1989, **78**, 312–315.

16 E. I. Goldyreva, I. A. Leonidov, M. V. Patrakeev and V. L. Kozhevnikov, *J. Solid State Electrochem.*, 2016, **16**, 1187–1191.

17 E. I. Leonidova, I. A. Leonidov, M. V. Patrakeev and V. L. Kozhevnikov, *J. Solid State Electrochem.*, 2011, **15**, 1071–1075.

18 B. V. Golovkin and G. V. Bazuev, *Russ. J. Gen. Chem.*, 2010, **80**, 213–218.

19 A. Bhaskar, C.-J. Liu and L.-C. Huang, *J. Electroceram.*, 2013, **31**, 129–133.

20 J. L. Chen, Y. S. Liu, C.-J. Liu, L.-C. Huang, C. L. Dong, S. S. Chen and C. L. Chang, *J. Phys. D: Appl. Phys.*, 2009, **42**, 135418–135423.

21 V. G. Zubkov, G. V. Bazuev, A. P. Tyutyunnik and I. F. Berger, *J. Solid State Chem.*, 2001, **160**, 293–301.

22 C. H. Hervoches, H. Okamoto, A. Kjekshus, H. Fjellvåg and B. C. Hauback, *J. Solid State Chem.*, 2009, **182**, 331–338.

23 G. V. Bazuev, V. G. Zubkov, I. F. Berger and V. N. Krasil'nikov, *Russ. J. Inorg. Chem.*, 2001, **46**, 317–322.

24 N. Kanas, S. P. Singh, T. D. Desissa, T. Norby, K. Wiik, T. Grande and M.-A. Einarsrud, *Materials*, 2019, **12**, 497–507.

25 T. D. Desissa, N. Kanas, S. P. Singh, K. Wiik, M.-A. Einarsrud and T. Norby, *Phys. Chem. Chem. Phys.*, 2018, **20**, 2754–2760.

26 M. Chen, B. Hallstedt and L. J. Gauckler, *J. Phase Equilib.*, 2003, **24**, 212–227.

27 G. Kresse and D. Joubert, *Phys. Rev. B: Condens. Matter Mater. Phys.*, 1999, **59**, 1758–1775.

28 G. Kresse and J. Furthmüller, *Phys. Rev. B: Condens. Matter Mater. Phys.*, 1996, **54**, 11169–11186.

29 J. P. Perdew, K. Burke and M. Ernzerhof, *Phys. Rev. Lett.*, 1996, **77**, 3865–3868.